Title: Multimodal gradients of human basal forebrain connectivity

Authors: Sudesna Chakraborty*[1,2], Roy A.M. Haast[2,6,7], Kate M. Onuska[1,2,4] , Prabesh Kanel[8,9,10], Ali R. Khan[1,2,5], Taylor W. Schmitz*[2,3,4]

[1]Neuroscience Graduate Program, Western University, London, Ontario Canada

[2]Robarts Research Institute, Western University, London, Ontario Canada

[3]Department of Physiology and Pharmacology, Western University, London, Ontario Canada

[4]Lawson Health Research Institute, Western University, London, Ontario Canada

[5]Department of Medical Biophysics, Western University, London, Ontario Canada

[6]Aix Marseille Univ, CNRS, CRMBM, Marseille, France

[7]APHM, Hôpital Universitaire Timone, CEMEREM, Marseille, France

[8]Department of Radiology, University of Michigan, MI, Ann Arbor, USA Morris K.

[9]Morris K.Udall Center of Excellence for Parkinson's Disease Research, University of Michigan, Ann Arbor, MI, USA

[10]Parkinson's Foundation Research Center of Excellence, University of Michigan, Ann Arbor, MI, USA

Correspondence to: *Sudesna Chakraborty; *Taylor W. Schmitz

Email: schakr28@uwo.ca; tschmitz@uwo.ca

Author Contributions: Author contributions: S.C., A.R.K. and T.W.S designed research; S.C., R.A.M.H., and A.R.K. performed research; A.R.K., and R.A.M.H. contributed new reagents/analytic tools; PK preprocessing of PET image, review and critique; S.C., and R.A.M.H. analyzed data; and S.C. and T.W.S. wrote the paper

Competing Interest Statement: no conflict of interest.

Classification: Biological Sciences, Neuroscience

Keywords: Basal Forebrain, Connectivity, Human, Neuroimaging

Abstract

The cholinergic innervation of the cortex originates almost entirely from populations of neurons in the basal forebrain (BF). Structurally, the ascending BF cholinergic projections are highly branched, with individual cells targeting multiple different cortical regions. However, it is not known whether the structural organization of basal forebrain projections reflects their functional integration with the cortex. We therefore used high-resolution 7T diffusion and resting state functional MRI in humans to examine multimodal gradients of BF cholinergic connectivity with the cortex. Moving from anteromedial to posterolateral BF, we observed reduced tethering between structural and functional connectivity gradients, with the most pronounced dissimilarity localized in the nucleus basalis of Meynert (NbM). The cortical expression of this structure-function gradient revealed progressively weaker tethering moving from unimodal to transmodal cortex, with the lowest tethering in midcingulo-insular cortex. We used human [^{18}F] fluoroethoxy-benzovesamicol (FEOBV) PET to demonstrate that cortical areas with higher concentrations of cholinergic innervation tend to exhibit lower tethering between BF structural and functional connectivity, suggesting a pattern of increasingly diffuse axonal arborization. Optogenetic tracing of cholinergic projections and [^{18}F] FEOBV PET in mice confirmed a gradient of axonal arborization across individual BF cholinergic neurons. Like humans, cholinergic neurons with the highest arborization project to cingulo-insular areas of the mouse isocortex. Altogether, our findings reveal that BF cholinergic neurons vary in their branch complexity, with certain

47 subpopulations exhibiting greater modularity and others greater diffusivity in the
48 functional integration of their cortical targets.

Introduction

The basal forebrain (BF) (Fig. 1) is a collection of subcortical cholinergic cell groups which provide the major sources of acetylcholine to the cortex and hippocampus[1]. Structurally, the ascending cholinergic projections are highly branched, with individual cells often targeting multiple different cortical areas[2–4]. The total arborization of a single human cholinergic BF neuron is estimated to have a length in excess of 100 meters[4].

The organization of ascending BF cholinergic projections may reflect complex spatial topographies of connectivity with the cortex[5,6]. Axonal tracing studies in rats suggest that BF cholinergic neurons are grouped into ensembles which target functionally interrelated cortical areas[7]. In humans, patterns of functional connectivity in distinct BF subregions have been found to overlap with distinct cortico-cortical networks[8–10]. Consistent with a spatial topography of projections, subregional structural changes in BF gray matter and white matter integrity are associated with distinct patterns of cortical degeneration and cognitive dysfunction[11–15]. In neurodegenerative diseases such as Alzheimer's (AD), early dysfunction or loss of specific BF cholinergic fibers may alter local neuronal functions in cholinoreceptive cortical areas[16]. Although these separate lines of evidence suggest that the cortex expresses topographies of BF structural and functional connectivity, the intermodal relationship of these topographies to one another is unknown.

How does the structural organization of cholinergic BF projections relate to their functional integration in the cortex? One possibility is that gradients of BF structural and functional connectivity are closely tethered. This would be expected if white matter tracts emanating from local populations of BF cholinergic neurons target local patches of cortex, with each axonal projection exhibiting relatively uniform branch complexity of its terminal fields[5]. In this scenario, BF functional connectivity would reflect these structurally segregated cortical modules. Alternatively, gradients of BF structural and functional connectivity might exhibit negligible overlap. This pattern would be expected if populations of BF cholinergic neurons project diffusely to multiple distinct and overlapping cortical areas[5]. In this scenario, BF functional connectivity would reflect mixtures of these diffuse afferent inputs. Finally, a third possibility is that the profile of tethering between gradients of BF structural and functional connectivity itself falls along a gradient. This pattern would be expected if populations of BF cholinergic neurons vary in their branch complexity, with certain subpopulations exhibiting greater modularity and others greater diffusivity in the functional integration of their cortical targets.

Here we addressed the relationship between structural and functional connectivity in the ascending BF projections. We used multimodal imaging combining high-resolution 7 Tesla (7T) diffusion (dMRI) and resting state functional MRI (rsfMRI) in a cohort of 173 individuals from the Human Connectome project (HCP)[17]. From these datasets, we derived gradients of the continuous transitions in BF functional and structural connectivity with the cortex. In both modalities, a single gradient dominated

90 the explained variance in connectivity, characterized by an anteromedial to
91 posterolateral axis spanning the BF nuclei. To quantify BF structure-function tethering
92 directly, we computed the residual variance between (a) the gradients of structural and
93 functional connectivity within the BF and (b) the expression of these gradients on the
94 cortical surface. Consistent with a gradient of branch complexity across the BF, we
95 found closer tethering between BF structural and functional connectivity in medial areas
96 of the BF, with stronger divergence in posterolateral areas overlapping the nucleus
97 basalis of Meynert (NbM). The cortical expression of this structure-function tethering
98 was weakest in midcingulo-insular hubs of the ventral attention network[18–26]. Using *in*
99 *vivo* molecular imaging of the human and mouse cortical cholinergic projections, in
100 combination with mouse optogenetic labeling of individual BF cholinergic projections,
101 we provide cross-species translational evidence that the observed gradient of tethering
102 between BF structural and functional connectivity is likely shaped by the complexity of
103 axonal arborization in BF cholinergic neurons. In mouse and human, BF cholinergic
104 neurons with greater arborization appear to target evolutionarily conserved midcingulo-
105 insular cortical areas.
106

107 **Results**

108 Primary BF structural and functional gradients

109 We built dMRI and rsfMRI connectomes of the BF using high-resolution 7T MRI
110 HCP data (n=173)[27] and a well-validated stereotactic BF atlas which provides

111 annotations for its separate nuclei (Fig. 1)[28]. For each individual, the structural and
112 functional connectomes were separately defined by an *M*-by-*N* matrix, where *M*
113 represents the voxels in the entire BF and *N* represents the cortical parcels of the HCP
114 multimodal parcellation (HCP-MMP)[29]. For rsfMRI data, the matrices encode the
115 interregional temporal correlations in blood oxygenation level-dependent signals. For
116 dMRI data, the matrices encode the streamline counts between different regions of the
117 brain and BF. We confirmed that the probabilistic tractography of the BF streamlines
118 recapitulates prior ex vivo anatomical tracing[30] and in vivo diffusion mapping[14,31] work
119 on the human BF projectome which distinguish midline cingulum and lateral
120 capsular/perisylvian white matter projection routes (Supplemental Fig. 1).

121 For each modality, we computed gradients of connectivity using the BrainSpace
122 toolbox[32]. Starting from the input matrices encoding the rsfMRI and dMRI data
123 (averaged across individuals), we used a kernel function to build an affinity matrix
124 encoding interregional similarity of features. These matrices were decomposed via
125 nonlinear dimension reduction into a set of eigenvectors describing axes of BF
126 connectivity with cortical targets. The axes were then projected back to the BF space
127 (Supplemental Fig. 2A).

128 The first gradient for both BF structural and functional connectivity data
129 explained the most (30%) variance followed by a reduction in explained variance by 50%
130 for the second gradient (Fig. 2A). We therefore focused on the first principal gradient in
131 each modality. In both the structural and functional gradient, a smooth gradient

132 transition from anteromedial to posterolateral BF was observed (Fig. 2B,C). The
133 connectivity profiles are consistent with findings from histological mapping of the
134 individual BF nuclei [12,28] and in prior cluster-based parcellations of the BF from rsfMRI[8–
135 10]. Note that the hemispheric asymmetry in these gradients is due to the original
136 stereotaxic mapping of the BF atlas (Fig. 2B; Methods).

137 We next computed gradient-weighted cortical maps[33] to determine how BF
138 gradients were expressed by the cortex. The gradient-weighted cortical maps were
139 created by multiplying each row of the initial connectivity matrix ($M_{\text{BF voxels}}$ x N_{cortical}
140 $_{\text{parcels}}$) with the corresponding structural principal gradient (sG1) or functional principal
141 gradient (fG1) value to create a gradient-weighted connectivity matrix. Finally, all rows
142 of this gradient-weighted matrix were averaged to produce a single cortical
143 representation of the particular gradient (see Supplemental Fig. 2B and Methods). For
144 the gradient-weighted cortical map corresponding to sG1 (sG1ctx; Fig. 2D left), we
145 observed a smooth macroscale transition from the anteromedial to posterolateral
146 cortical surface. By contrast, the gradient-weighted cortical map corresponding to fG1
147 (fG1ctx; Fig. 2D right) exhibited a more patch-like pattern with moderate differentiation
148 of gradient weights between midline and lateral cortical areas.

149 <u>A gradient of structure-function tethering in BF connectivity</u>

150 We next examined the magnitude of shared variance, or tethering, between BF
151 structural and functional gradients to determine their spatial similarity to one another.
152 To do so, we computed voxel-wise regressions for the fG1 and sG1 structure-function

153 gradient pair and extracted their corresponding residuals (see Methods). The residual
154 map encoding BF structure-function tethering was projected back to BF space, which
155 revealed an anteromedial to posterolateral topography, with the lowest structure-
156 function tethering localized in posterolateral subregions (Fig. 2E). We next computed
157 the gradient-weighted cortical map encoding our residualized map of BF structure-
158 function tethering. The resulting cortical map (Fig. 2F) exhibited decreased tethering
159 moving from unimodal to transmodal cortex, with lowest tethering in the anterior
160 cingulate, insular and frontal opercular cortices.

161 How does the smooth transition of tethering between BF structural and
162 functional connectivity (Fig. 2E) align with the histologically defined boundaries of the
163 BF anteromedial (Ch1,2,3) and posterolateral (Ch4,4p) nuclei (Fig. 2B)[28]? To address this
164 question, we examined if the distributions of residual values within Ch1,2,3 and Ch4,4p
165 differed from one another. We performed permutation tests with fitted surrogate maps
166 (see Methods) to compute the difference in both the means and dispersion between
167 Ch1,2,3 and Ch4,4p. Dispersion was quantified by the coefficient of variation (CoV)
168 defined as the ratio of the standard deviation to the mean of the data. The mean
169 residual values were not different between Ch1,2,3 and Ch4,4p (p_{perm}=0.40). However,
170 the residual values in Ch4,4p exhibited significantly greater variability in comparison to
171 Ch1,2,3 (p_{perm}=0.01). This latter finding suggests that structure-function tethering within
172 Ch4,4p was more inhomogeneous than Ch1,2,3 (Fig. 3A).

173 We then asked how well the cortical residual-weighted map of BF structure-
174 function tethering (Fig. 2F) aligns with the spatial topographies of intrinsic cortico-
175 cortical resting state networks. To do so, we compared the mean and CoV of the
176 distributions of residual values captured by each of 7 Yeo macroscale resting state
177 networks[25] covering the entire human cerebral cortex. A pattern in which the
178 distributions of these residual values are well delineated from one another across the
179 different cortico-cortical networks (distinct means, lower CoVs) would indicate that each
180 network falls along a continuum of BF structure-function tethering defined by the
181 observed anteromedial-to-posterolateral gradient. By contrast, a pattern in which the
182 distributions of residuals are more spread out across the different cortico-cortical
183 networks (overlapping means, higher CoVs) would indicate that each network exhibits a
184 mixture of lower and higher BF structure-function tethering. We found that the mean of
185 the residuals significantly differed among networks ($F_{6,330}$ =47.55, p=0.001, Fig. 3B), with
186 the ventral attention network characterized by significantly higher values than the visual
187 (p=0.001) and somatomotor networks (p=0.001). The dorsal attention, limbic,
188 frontoparietal and default mode networks exhibited an intermediate tendency for
189 structure-function tethering. However, we also observed that the CoVs captured by
190 each cortico-cortical network also differed ($F_{6,330}$=47.55, p=0.001). Again, the ventral
191 attention network exhibited significantly greater heterogeneity in residual values than
192 the visual (p_{perm}=0.001) and somatomotor networks (p_{perm}=0.001; Fig. 3B). Taken
193 together, these findings support a continuum of BF structure-function tethering.

194 Cortico-cortical networks with hubs primarily in the unimodal cortex (visual,
195 somatomotor) tend to exhibit higher tethering, while networks with hubs primarily in
196 the transmodal cortex tend to exhibit lower tethering .

197 To assess the stability of the dominant structural and functional connectivity
198 gradients (sG1 and fG1) and the gradient of their tethering, we performed cross-
199 validation analyses across the 173 individuals in the sample (see Methods). We found
200 that each individual's observed gradients were consistently highly correlated with the
201 model (split-half or leave-one-out), consistent with stable gradient organization across
202 individuals (Supplemental Fig. 3).

203 Having confirmed the stability of sG1, fG1, and their tethering across individuals,
204 we next examined if gradients with lower explained variance, e.g. sG2 and fG2, may
205 reveal additional profiles of BF structure-function tethering. To explore this possibility,
206 we computed the 'knee-point' in the curve of explained variance for the complete set of
207 observed structural and functional gradients (see Methods), where the change in
208 explained variance became negligible[34]. The knee-point corresponded to sG6 for
209 structural gradients and fG4 for functional gradients (Fig 2A, red versus blue color
210 gradient component). For each of the 24 structure-function gradient pairs in this 6 x 4
211 cross-modality gradient matrix (Supplemental Fig. 4A), we computed the structure-
212 function tethering metric as before. When we examined the average of the 24 residual
213 maps (Supplemental Fig. 4B), we observed a high degree of correspondence to the sG1-
214 fG1 residual map (r=0.918; Supplemental Fig. 4C), even when excluding sG1-fG1 pairing

215 from the average (r=0.878; Supplemental Fig. 4D). These findings imply that the gradient
216 of tethering between BF structural and functional connectivity is captured by a single
217 dominant profile (Fig. 2E).

218 BF structure-function tethering reflects an arborization gradient of cholinergic neurons

219 We next explored what properties of BF connectivity might shape the observed
220 gradient profile of structure-function tethering in the cortex. Currently, [^{18}F]FEOBV
221 positron emission tomography (PET) provides the most direct *in vivo* assay of cortical
222 cholinergic innervation in humans. The [^{18}F]FEOBV radiotracer binds to the vesicular
223 acetylcholine transporter (VAChT), a glycoprotein expressed solely by cholinergic
224 neurons, with the highest density of expression on the presynaptic terminals [35]. We
225 acquired distribution volume ratios (DVR) of [^{18}F]FEOBV binding from a group of healthy
226 cognitively normal young adults (*n*=13; mean age=24.54, 3 females)[36], and produced an
227 average map representing the BF cortical cholinergic projectome (Fig. 4A; see Methods).
228 We then examined the correlation between the cortical expression of BF structure-
229 function detethering (cortical residual map from Fig. 2F) and cholinergic innervation
230 estimated from the average [^{18}F]FEOBV map using spatial spin tests[37]. Surprisingly, we
231 found that cortical areas exhibiting lower BF structure-function tethering, i.e., more
232 branching, exhibited a higher density of BF cholinergic input, i.e., higher VAChT
233 concentration (R=0.28, p_{spin}=0.02; Fig. 4B). We replicated these associations with three
234 other publicly available atlases of [^{18}F]FEOBV PET [38–40] and found similar strong positive
235 relationships (Supplemental Fig. 6).

236 Why might BF structural and functional connectivity diverge in cortical regions
237 more densely innervated by BF cholinergic input? One possibility is that cortical areas
238 expressing lower tethering between BF structural and functional connectivity tend to
239 receive inputs from more highly branched cholinergic neurons. Under this 'arborization
240 gradient' account, these cortical areas would exhibit strong BF functional connectivity
241 and dense VAChT expression from multiple converging collateral arbors, but relatively
242 weak structural connectivity due to greater diffusivity in the ascending tracts. To test
243 this hypothesis, we computed seed-based connectivity of the BF with each HCP-MMP
244 cortical parcel for both the rsfMRI (Pearson r-values) and dMRI (streamline counts)
245 datasets, and then projected these to the cortical surface. For the cortical estimate of BF
246 seed-based connectivity in each modality, we examined its spatial relationship with
247 cortical VAChT concentration. Consistent with an arborization gradient, we observed a
248 significant positive relationship of cortical VAChT concentrations with BF functional
249 connectivity ($R=0.501$, $p_{spin}=0.002$), but not structural connectivity ($R=-0.118$,
250 $p_{spin}=0.549$; Fig. 4C). Moreover, the relationship of BF functional connectivity with
251 cortical VAChT was significantly stronger than that observed for BF structural
252 connectivity (average difference of 0.608 between correlation coefficients with 95% CI
253 [0.727, 0.493], $p_{boot}<0.001$, as revealed by bootstrap analysis), with the greatest
254 divergence between the two modalities in cortical parcels with higher VAChT
255 concentrations.

256 If the arborization of BF cholinergic neurons differs depending on the cortical
257 target of their projections, this pattern may reflect the cortical target's function
258 (unimodal versus transmodal) and biophysical constraints on the cholinergic projection
259 itself. The brain organizes its connections to optimize communication while minimizing
260 the biological resources required for these connections, or 'wiring cost'[41–43]. Neurons
261 with long-range projections which extend from one brain region to another therefore
262 often have fewer axonal branches than neurons with shorter-range projections. The BF
263 cholinergic neurons may therefore balance the total distance traveled by their
264 ascending axonal projections with the total number of axonal arborizations. To test this
265 hypothesis, we used the diffusion tractography data to compute the average white
266 matter fiber length from the BF ROI to each cortical parcel (Methods). The fiber length
267 estimates were then projected to the cortical surface (see Methods, Fig. 5A) and
268 compared to BF structure-function tethering using spin tests [37,44]. Consistent with a
269 distance/arborization tradeoff, we detected a significant negative relationship where
270 cortical areas receiving longer fibers tend to exhibit closer structure-function tethering
271 ($R=-0.280$, $p_{spin}=0.027$, Fig. 5B) and lower VAChT concentration ($R=-0.483$, $p_{spin}=0.004$,
272 Supplemental Fig. S6). When examining the separate relationships of BF structural
273 connectivity (stream-line counts) and functional connectivity (Pearson r-values) with
274 fiber lengths (Fig 5C), we found that cortical areas which receive longer fibers tend to
275 express higher streamline counts ($R=0.455$, $p_{spin}=0.0003$). This relationship was
276 significantly stronger than that observed between fiber length and resting state

277 correlations with the BF (R=-0.226, p_{spin}=0.455) with a difference of -0.771 between
278 correlation coefficients (95% CI [-0.664, -0.881], p_{boot}<0.001).

279 These findings are consistent with a pattern in which more individual BF neurons
280 (with high wiring costs) are needed to innervate distal cortical regions due to lower
281 branching. We therefore next computed an estimate of BF wiring cost[45,46] by multiplying
282 the average fiber length with the total number of streamlines received from the BF for
283 each MMP cortical parcel. In this fiber distance-weighted structural connectivity map
284 (Figure 6A), the further away and the stronger the structural connectivity, the larger the
285 wiring cost. Expectedly, the highest wiring costs were observed in cortical areas which
286 receive input from cholinergic neurons predicted to have the lowest branching, e.g.
287 primary visual and somatomotor cortex. These cortical areas also tend to have the
288 farthest geodesic distances from the BF (Figure 6B).

289 Cellular evidence for a gradient of arborization in BF cholinergic neurons

290 Thus far, the distance/arborization tradeoff observed in humans implies that the
291 branch complexity of individual cholinergic neurons is shaped by a combination of the
292 physical proximity and function of its cortical targets. However, a limitation of human *in*
293 *vivo* MRI is that it cannot resolve single cell axonal branching of cholinergic neurons. To
294 test the arborization gradient hypothesis more directly, we leveraged a whole brain
295 atlas of mouse BF cholinergic projections[2] derived from cell-type specific optogenetic
296 labeling of individual BF cholinergic soma and axonal projections (Supplemental Fig.
297 S7A). For each neuron, the targets of its axonal branches were labeled using the Allen

298 Mouse Brain Atlas[47], and classified according to whether any one of their branches
299 targeted transmodal (iso)cortical areas. We identified 7/50 neurons fitting this criterion
300 and extracted the annotations corresponding to their cortical targets from the 3D Allen
301 Mouse Brain Atlas (Fig 7A). The target areas include infralimbic and cingulate cortical
302 areas within the mouse homologue of the salience network[48,49]. The remaining 43
303 neurons target unimodal sensory, motor or subcortical areas.

304 We next counted the number of distinct brain-wide targets for each of the 50 BF
305 cholinergic neurons. There was substantial variation in branch counts, ranging from
306 neurons with only a single target to neurons with up to 12 different targets across the
307 brain (Fig 7B). A permutation test comparing the number of branches between these
308 two sets of neurons (transmodal targeting versus unimodal/subcortical targeting)
309 revealed significantly higher branch counts in the transmodal targeting subset (10k
310 permutation, $t=3.2$, $p_{perm}=0.004$). To compare the distributions of BF neuronal branching
311 in mice with our metric of BF neuronal branching in humans (structure-function
312 tethering), we sorted the BF residuals (Figure 7C inset) from low to high across the 599
313 voxels comprising the full BF ROI. Consistent with mice, the distribution was right-
314 skewed with a small concentration of higher residual values and a long left tail of
315 smaller values (Fig 7C). For mouse and human, we split the respective distributions of
316 neuronal branching and voxel residuals into tertiles to examine the concentrations of
317 values (higher versus lower) relative to the total number of observations. For mice, the
318 highest tertile contained only a small percentage (4%) of neurons with > 8 branches (Fig.

319 7D). Similarly for humans, the highest tertile contained a relatively small percentage
320 (13%) of BF voxels (Fig. 7E). In both species, BF cholinergic neurons with very high
321 branching thus represent a relatively smaller proportion of the total neuronal
322 population. The shapes of the continuous distributions for single cell branch counts (Fig
323 7B) and for voxel residuals (Fig 7C) were also highly similar to one another (Spearman's
324 rank correlation = 0.975; Fig 7F), despite the fact that they originate from separate
325 species and measurement techniques.

326 To bridge the gap between measures of central cholinergic innervation in human
327 and mouse, we acquired *in vivo* [^{18}F]FEOBV PET data in wild-type (WT) mice (n=11) and
328 quantified VAChT concentrations in the salience network regions (Fig. 7A) identified by
329 the prior optogenetic tracing study[2] and a control region of interest comprising Allen
330 Mouse Brain Atlas annotations for the visual cortex (see Methods, Supplemental Fig.
331 S7B). In humans, we extracted [^{18}F]FEOBV PET measures of VAChT from the homologous
332 ventral attention and visual networks, as defined from the a priori Yeo [25] networks (Fig.
333 3B). In both mice and humans, we found that VAChT concentrations were significantly
334 higher in salience network hubs compared to the visual cortex (Fig. 7G; mouse:
335 t_{10}=11.54, p<0.0001; human: t_{12}=17.19, p<0.0001). These findings provide further
336 translational evidence that BF cholinergic neurons exhibit an arborization gradient
337 which is shaped by the function and physical distance of their cortical targets.

338 To emphasize the features capturing the BF cholinergic arborization gradient in
339 humans, we generated a cortical surface integrating measures of (1) BF structure-

340 function tethering, (2) cortical VAChT concentration, and (3) fiber lengths of BF white
341 matter projections (Methods, Fig. 8A). The highest convergence of these three features
342 selectively colocalizes midcingulo-insular hubs of the ventral attention network (white
343 boundaries). Altogether, our findings accord with a gradient of BF cortical cholinergic
344 innervation which captures both modular (more neurons, fewer branches) and diffuse
345 (fewer neurons, more branches) properties of functional integration[5], depending on the
346 subregional point of origin within the BF and the cortical targets (Fig. 8B).
347

348 **Discussion**

349 We examined how the structural organization of cholinergic BF projections
350 relates to their functional integration in the human and mouse cortex. Our findings,
351 derived from multimodal in vivo brain imaging and cell type specific tracing of BF
352 cholinergic axons, imply that the branch complexity of cholinergic projections may
353 reflect properties of the cortical areas they target. Moving up the cortical hierarchy,
354 neuronal populations with both increasingly diverse repertoires of cortical-cortical
355 connectivity and shorter projection distances from the BF receive input from
356 increasingly branched BF cholinergic neurons.

357 We considered the spatial relationship of the BF arborization gradient (defined
358 from the residuals between BF structural and functional connectivity) to an established
359 set of the brain's core resting state networks[25]. Our findings indicate a pattern of
360 cortical cholinergic innervation where shifts in axonal branching align spatially with

361 boundaries of cortico-cortical network hubs. Cholinergic neurons with the highest
362 arborizations target hubs of the midcingulo-insular network. Moving down this
363 arborization gradient, frontoparietal and temporal network hubs exhibit an innervation
364 profile of intermediate branching. Finally, cholinergic neurons with the fewest arbors
365 per cell appear to preferentially target unimodal sensory cortices. In this hierarchically
366 organized projection pattern, cholinergic neurons with fewer branches would need to
367 be more numerous than those with many branches in order to provide coverage of an
368 equivalent cortical surface area. Consistent with this prediction, cortical areas which
369 receive higher numbers of BF streamlines tend to be farther away from the BF in terms
370 of fiber lengths (Fig. 5C). Moreover, when we split estimates of axonal branch counts
371 into tertiles in both mouse (cells) and human (voxels), the lowest tertile comprised >60%
372 of observations (Fig. 7D,E), while the uppermost tertile comprised <15%. Hence, the BF
373 appears to be populated by a significantly larger proportion of neurons with relatively
374 fewer branches.

375 What is the functional significance of a cholinergic arborization gradient in this
376 hierarchical cortical architecture? Neuroimaging work examining the functional and
377 structural connectivity of the brain's cortico-cortical networks has consistently identified
378 the midcingulo-insular in high level selection and enhancement of both exogenous
379 (sensory) and endogenous sources of input[18–26]. These two streams of information are
380 thought to reflect a fundamental division of labor in the brain's network organization.
381 Support for this division comes from work demonstrating that exogenous and

382 endogenous networks tend to be functionally anticorrelated with one another[50–54],
383 reflecting their competitive interactions for representational dominance of the outside
384 sensory world versus internal mental content. The midcingulo-insular areas are unique
385 in that they exhibit positive temporal correlations with networks in both the exogenous
386 and endogenous processing streams, implying a superordinate role in selecting between
387 the two[26,55–57]. We also recently provided meta-analytic evidence that task-related
388 midcingulo-insular activations, as measured by fMRI, exhibit among the strongest
389 patterns of pharmaco-modulation by cholinergic agonists and task-related co-
390 activations with the BF[58]. The profile of BF cholinergic arborization and strength of its
391 modulatory regulation on midcingulo-insular cortex provide further evidence of its
392 privileged supervisory status.

393 Cortical cholinergic signaling is thought to play a central role in promoting the
394 selection and processing of relevant stimuli while suppressing competing irrelevant
395 information[5,59–61]. Parallel lines of research in mouse and non-human primates has
396 started to uncover the cortical circuit and computation which enable this core property
397 of brain function[62]. The BF cholinergic inputs form an integral component of a canonical
398 disinhibitory microcircuit expressed throughout the cortex, composed of pyramidal
399 neurons and multiple classes of interneurons[63–71], possibly organized at the columnar
400 scale[72,73]. Targeted release of acetylcholine in this microcircuit may bias mutually
401 suppressive responses of neuronal populations competing for attentional resources
402 [62,74–76], allowing one population to dominate over others. Moving up the cortical

403 hierarchy, individual cholinergic neurons may require larger arborizations to bias
404 competitive responses across increasingly large and spatially distributed populations of
405 cortical neurons. We speculate that coalitions of BF cholinergic neurons may coordinate
406 the release of acetylcholine[77,78] along this arborization gradient. These transient
407 coordinated patterns of signaling may act to flexibly segregate[79] assemblies of
408 neurons[80–83] across the cortical hierarchy to form coherent attentional episodes [84].

409 A diversity of branch complexity in BF cholinergic neurons may also account for
410 differences in their vulnerability to aging and disease. Cell type specific labeling and
411 transcriptomic analyses examining morphological and functional properties which
412 increase a neuron's vulnerability to age-related neurodegenerative disease such as AD
413 have consistently demonstrated large axonal projections as a key risk factor [4,85–87]. The
414 observed decreased structure-function tethering in the postero-lateral BF, and in
415 particular the NbM, is consistent with neurons exhibiting large arborizations. This
416 morphofunctional property of NbM cholinergic neurons may increase their vulnerability
417 to dysfunction in the aging brain. In parallel, our observation that ventral attention
418 network may receive input from the most highly branched NbM cholinergic neurons
419 implies that these cortical areas might exhibit higher vulnerability to dysfunctional
420 cholinergic signaling in the aging brain. It is also notable that the BF cholinergic neurons
421 with fewer arborizations, which our findings suggest primarily target the primary and
422 somatosensory cortices, constitute projection zones which are relatively spared by
423 pathology in early stages of AD [88].

424 Our findings are subject to several important methodological considerations.
425 First, the basal forebrain is a small subcortical structure with poorly defined anatomical
426 boundaries. We therefore used a probabilistic atlas to localize its constituent nuclei.
427 However, when using probabilistic BF atlases in combination with data collected at
428 spatial resolutions typical of 3T structural (1.5 mm^3) and functional MRI (3 mm^3),
429 aliasing of adjacent structures has been shown to systematically overestimate the BF
430 gray matter[89]. To mitigate this issue, we used optimized MRI protocols to acquire high
431 spatial resolution dMRI (1.05 mm^3) and rsfMRI (1.6 mm^3) at 7T [90,91]. Second, our
432 measures of structural connectivity were estimated using streamline tractography on
433 diffusion-weighted imaging, which can be susceptible to false positives and negatives in
434 certain brain areas[89]. It is therefore possible that the regional variation in BF structure–
435 function correspondence is partly explained by regional variation in tractography
436 performance. Another concern is the susceptibility-related spatial distortions near the
437 BF region for fast readout scans, such as those used for the rsfMRI acquisitions by the
438 HCP. Although corrected for using a separately acquired field map, these spatial
439 distortions might lead to suboptimal probing of BF voxels in such data with possible
440 contamination from white matter (WM) tissue and cerebro-spinal fluids (CSF). To limit
441 the impact of the latter on the functional time series analysis, additional denoising using
442 the average WM and CSF timeseries was performed.

443 In sum, we demonstrate that multimodal gradients of BF connectivity reveal
444 spatially inhomogeneous patterns of structure-function tethering in the cortex, with the

445 lowest tethering in mid-cingulate and anterior insular cortical areas involved in salience
446 detection and allocation of attentional resources throughout the brain. These cortical
447 areas tend to be located proximal to the BF and receive disproportionately higher
448 concentrations of cholinergic innervation. Our findings conform to a model in which this
449 multimodal BF gradient is shaped in part by axonal branch complexity.
450

451 **Materials and Methods**

452 We used high-resolution minimally pre-processed 7T MRI HCP data (n=173)[27]
453 and the existing stereotactic atlas of the BF [28] to build structural and functional
454 connectomes. Any further pre- and postprocessing was done on the high-performance
455 computing cluster of the Digital Research Alliance of Canada. Workflows were built
456 using Snakemake[92] with the full workflow available on GitHub (see data and code
457 availability for specifics). Individual connectomes were averaged and reduced to a 2-
458 dimensional *M*-by-*N* matrix describing the pairwise connectivity strength between *M* BF
459 ROI voxels and *N* cortical regions[29]. The BrainSpace toolbox[32] was used to capture the
460 gradients which, as well as any further analysis, was done using Jupyter Notebooks [93].

461 <u>Human Data Acquisition</u>

462 High-resolution 7T dMRI and rsfMRI data were downloaded from the HCP data
463 repository [17]. We used the minimally pre-processed data (described in ref [27]) consisting
464 of 173 healthy subjects (69 male, 104 female) aged 22 to 35 years. The dMRI images
465 were collected with a 1.05 mm^3 isotropic voxel size, TR=7000 ms, TE=71.2 ms, b-

466 values=1000, 2000 s/mm^2 , FOV=210 x 210 mm^2. Resting-state fMRI images were
467 collected with a 1.6 mm^3 isotropic voxel size, TR=1000 ms, TE=22.2 ms, FOV=208 mm^2,
468 spanning 4 runs of 16-minute duration each, per subject. For anatomical imaging, two
469 T_1-weighted (T_1w) scans were obtained using a three-dimensional (3D) magnetization-
470 prepared rapid gradient-echo (MPRAGE)[94] sequence with identical geometries and a 0.7
471 mm^3 isotropic voxel size. Full details of the acquisition parameters can be found in the
472 HCP S1200 release reference manual [95].

473 Basal Forebrain Mask

474 The BF ROI was created using the existing stereotactic atlas of the BF [28]. This
475 stereotactic BF atlas is based on histological sections obtained from 10 postmortem
476 brains. The magnocellular cell groups were delineated in each slice, 3D reconstructed
477 and warped into the MNI single-subject reference space[96]. The atlas consists of 4
478 subregions of the BF defined in the nomenclature: Ch1-2, Ch3, Ch4, and Ch4p[97]. For
479 each subregion, a stereotactic probabilistic map has a range of 0 to 10 indicating the
480 number of brains containing the specific magnocellular cell groups in the given voxel.
481 Note that this atlas is not left, right symmetrical; hence, our BF ROI is asymmetrical. Our
482 BF ROI is created by thresholding these subregion masks to 50% first and then
483 combining all to get a mask covering full BF. This BF ROI mask was then warped into
484 MNI152 non-linear 6th generation atlas (MNI152Nlin6Asym) [96].

485 Structural Connectivity Reconstruction

486 Diffusion tractography was performed to get a connectivity matrix for diffusion
487 data. As part of the minimal preprocessing pipeline data release, all subjects underwent
488 FreeSurfer processing (v5.3.0-HCP)[98]. The BF ROI mask was then first resampled and
489 transformed to the individual subjects' minimally preprocessed volume space (0.7mm^3).
490 Volumetric cortical labels were built by mapping the HCP-MMP 1.0 surface
491 parcellation[29] using Connectome Workbench's ribbon-constrained *label-to-volume-*
492 *mapping* function and FreeSurfer-derived surfaces. The BF ROI voxels were used as
493 seeds, and the 180 cortical regions in each hemisphere were combined and used as
494 targets to perform probabilistic tractography using FSL's *probtrackx* [99] with 5000
495 streamlines per BF ROI voxel. The resulting probability maps (Supplemental Fig. 1C) in
496 the BF quantified the number of streamlines that reached each target. The maps were
497 resampled to MNI space[100] and 1.6 mm^3 resolution to match the functional connectivity
498 data and reduced to a 2-dimensional *M*-by-*N* matrix, where *M* represents the voxels in
499 the BF ROI (599 voxels) and *N* is the cortical targets (180 each hemisphere) with their
500 corresponding number of streamlines. Additionally, the 'wiring cost' connecting the BF
501 ROI with the cortex was calculated by multiplying the number of streamlines with their
502 average length for each cortical target (Gollo et al. 2018). The *M*-by-*N* connectivity
503 feature matrix, as well as cortical wiring cost map for all 173 subjects were averaged to
504 calculate the gradients and wiring cost, respectively.

505 <u>Functional Connectivity Reconstruction</u>

506 First, the BF ROI mask in the minimally preprocessed volume space was
507 resampled to the 1.6 mm^3 isotropic voxel size of the rsfMRI data and added to the
508 subject's subcortical parcellation. A functional connectivity matrix was then created for
509 each subject by calculating the temporal correlation between BF voxels and cortical
510 ROIs. All four runs (i.e., two sets of 16 min. runs with posterior-to-anterior and anterior-
511 to-posterior phase-encoding) of the minimally preprocessed and ICA-FIX denoised
512 rsfMRI data[101] were used. Since the BF ROI is not included in the dense timeseries
513 provided by HCP, these were regenerated using the updated subcortical parcellation to
514 include the BF ROI voxels for further processing. Subsequent processing included ROI-
515 constrained subcortical smoothing to match the cortical sampling density using the
516 scripts provided by HCP [98], as well as additional signal filtering (i) based on the average
517 WM and CSF timeseries using *ciftify* [102] and (ii) by applying a Wishart filter as proposed
518 previously[103,104] to selectively smooth unstructured noise more than the structured
519 blood oxygenation level-dependent signal. Average cortical ROI timeseries
520 (concatenated across runs) were then extracted using the HCP-MMP 1.0 surface
521 parcellation[29]. The 2-dimensional *M*-by-*N* functional connectivity matrices were
522 constructed by calculating the Pearson's correlation coefficient for each BF ROI voxel
523 (*M*) to each of the cortical parcels (*N,* 180 each hemisphere) and averaged over all
524 subjects to calculate group-wise gradients.

525 <u>Gradient Calculation</u>

526 Connectivity gradients were calculated using the BrainSpace toolbox[32]. Group
527 averaged connectivity matrices were used as input to the *GradientMaps* function, using
528 the normalized angle kernel and diffusion map embedding approach. This nonlinear
529 dimension reduction method transforms the connectivity matrix into a low-dimensional
530 representation to construct connectivity gradients and their corresponding lambda
531 values (i.e., explained variance)[105]. BF voxels that are characterized by similar
532 connectivity patterns will have a gradient value closer together, whereas voxels with
533 litter or no similarity are farther apart. These gradients were then mapped back onto
534 the BF voxel space to visualize continuous transitions in functional and structural
535 connectivity patterns (Supplemental Fig. 2A).

536 In addition, gradient-weighted cortical maps were created by multiplying each
537 row of the BF-cortical connectivity matrix with the corresponding gradient value of that
538 BF voxel [106] (Supplemental Fig. 2B). The distribution of cortical gradient-weighted values
539 was then decomposed into seven functional networks[25] using the HCP-MMP 1.0
540 parcellation-based 7 Yeo networks as defined in ref [25,107]. These include the visual,
541 somatomotor, dorsal attention, ventral attention, limbic, frontoparietal, and default
542 mode network.

543 Residual values (structure-function tethering) for each of the BF voxels and HCP-
544 MMP parcels were calculated based on the regression between the structural against
545 the functional gradients for the BF and gradient-weighted cortical maps, respectively.

546 <u>Human [^{18}F]FEOBV PET</u>

547 [^{18}F]FEOBV PET acquisition and preprocessing is described in Kanel et al [108]. Each
548 individual [^{18}F]FEOBV PET image was intensity normalized to the subject's supratentorial
549 white matter uptake to create a parametric DVR [^{18}F]FEOBV PET image[36]. The original
550 PET atlases were transformed to *10k_fsavg* surface-space and parcellated to HCP-MMP
551 1.0[29]. The values of each cortical parcel encoding the relative concentration of
552 cholinergic nerve terminals were rescaled[109] and visualized on an inflated surface (Fig.
553 4A). Additional [^{18}F]FEOBV maps[38,39] were obtained from the Neuromap toolbox[44] to
554 examine the reproducibility of our results.

555 Mouse [^{18}F]FEOBV PET

556 All small-animal imaging procedures were conducted in accordance with the
557 Canadian Council of Animal Care's current policies and were approved by the University
558 of Western Ontario's Animal Care Committee (Animal Use Protocols: #2016-104, #2020-
559 163) and the Lawson Health Research Institute's Health and Safety board.

560 High-resolution 9.4T MRI and [^{18}F]FEOBV PET data were acquired at the Centre
561 of Functional and Metabolic Mapping (Agilent Animal MRI Scanner, Bruker) and the
562 Lawson Health Research Institute's Preclinical Imaging Facility (Inveon DPET, Siemens
563 Healthineers), respectively. Data were acquired in 11 (5 male, 6 female) WT mice
564 (VAChT$^{flox/flox}$ [110]; C57BL/6J) at 6 months of age.

565 *In vivo* dynamic [^{18}F]FEOBV PET data were acquired as 150-minute list-mode
566 emission scans, performed with a timing window of 3.432 ns and a 350–640 keV
567 discrimination energy range. Mice were anesthetized (1.5-2.0% isoflurane in 1.0 L/min

568 $O_{2\ (g)}$) and then injected intravenously with a ~20 Megabecquerel (MBq) dose of
569 [^{18}F]FEOBV. Data were binned into consecutive frames of increasing duration (n_{frames} =
570 43), consisting of 15 frames of 40 seconds, followed by 28 frames of 300 seconds. An
571 OSEM3D algorithm with two iterations and 18 subsets was used to reconstruct
572 [^{18}F]FEOBV PET images with the following parameters: matrix dimensions: 128 mm ×
573 128 mm × 159 mm; voxel resolution: 0.776 mm × 0.776 mm × 0.796 mm.

574 Parametric volume of distribution (V_T) images were estimated for each mouse by
575 fitting the whole-brain [^{18}F]FEOBV time-activity curves with the multi-time point
576 graphical analysis methodology described by [111], where an image-derived input function
577 (IDIF) served as the reference. The IDIF was obtained from a volume of interest placed in
578 the lumen of the left ventricle of the mouse heart [112], and the start of the linear portion
579 (t*) was determined from the curve fitting, where t* = ~11.33 minutes.

580 Pre-processing of mouse [^{18}F]FEOBV V_T images was performed using SPM12
581 (https://www.fil.ion.ucl.ac.uk/spm/software/spm12/) in MATLAB R2020b. Preparation
582 of [^{18}F]FEOBV V_T images included resizing, centering, and re-orienting the images to
583 follow the right-hand coordinate system (RAS). Each V_T image was then coregistered to
584 its corresponding native space MRI image using normalized mutual information. Finally,
585 all [^{18}F]FEOBV V_T images were cropped to the native space MRI bounding box
586 dimensions and nonlinearly warped to the study-specific anatomical mouse brain
587 template (see below). To parcellate mouse [^{18}F]FEOBV V_T images, we performed non-

588 linear registration of the study-specific mouse brain template to the annotated images
589 from the Allen Mouse Brain Atlas[47].

590 For anatomical MRI, mice were anesthetized (1.5-2.0% isoflurane in 1.5 L/min O_2
591 $_{(g)}$) and then positioned in the center of a 30 mm RF volume coil (Bruker). Four iterations
592 of magnetization transfer (MT)-weighted spoiled gradient-recalled echo (GRE) images
593 were acquired using a fast low angle shot 3D pulse sequence with the following
594 parameters: FOV = 16 mm x 16 mm x 10 mm; matrix dimensions: 128 x 128 x 8; voxel
595 resolution = 0.125 mm^3, slice thickness = 10 µm; TR = 30 ms; TE = 2.77 ms; FA = 9°; off-
596 resonance saturation = 4.5 kHz (Gaussian pulse = 10 ms duration); effective FA = 900° [113].

597 Pre-processing of mouse anatomical brain images was performed using SPM12
598 (https://www.fil.ion.ucl.ac.uk/spm/software/spm12/) in MATLAB R2020b. For each
599 mouse, the anatomical brain images (*n*=4) were first averaged, then resized, centered,
600 and re-oriented to follow the RAS. Using normalized-cross correlation, the images were
601 then coregistered to the mouse brain template from ref [114], bias corrected using
602 MICO[115], and then segmented using tissue prior probability maps for gray matter, WM,
603 and CSF tissue compartments. For each mouse, the tissue segments from this step were
604 combined to mask out the surrounding skull and tissue. Finally, the gray and white
605 matter segmentations were used to create nonlinear transformations for diffeomorphic
606 registration to a population specific average template using geodesic shooting [116].

607 Geodesic Distance

608 Geodesic distance along the cortical surface was calculated using the geodesic
609 library (https://github.com/the-virtual-brain/tvb-gdist) based on the algorithm that
610 approximates the exact distance along the shortest path between two nodes (or
611 vertices) on a triangulated surface mesh[117]. An average BF seed node was created for
612 the left and right hemispheres separately by (i) projecting the BF mask onto the
613 *59k_fs_LR* white matter surface of the individual subjects using Connectome
614 Workbench's *volume-to-surface-mapping* function, (ii) averaging across all subjects to
615 get a probability map, (iii) resampling to the *10k_fsavg* surface-space as suggested by
616 the HCP study (https://wiki.humanconnectome.org) and (iv) then by thresholding at 0.5
617 to obtain a final binary BF seed on the cortical surface. A distance value was then
618 assigned to each cortical vertex based on the minimum geodesic distance along the
619 *10k_fsavg* pial surface to the BF seed node to avoid the medial wall. To match with the
620 resolution of the cortical connectivity results, the geodesic distance map was
621 parcellated using the HCP-MMP 1.0 atlas as implemented in the neuromaps toolbox [44],
622 and rescaled to values between 0 and 1 [109].

623 Statistical analyses

624 Permutation tests with surrogate maps[118] were used to compute statistical
625 significance for the BF gradients and the distribution of residuals. BF gradient values for
626 structural and functional connectivities were first rescaled between 0 and 1 and
627 Euclidean distance was used to calculate the distance matrix among all voxels within the
628 original BF ROI[109]. Variograms were then permuted (N=1000) using the *SurrogateMaps*

629 function implemented in the BrainSpace toolbox [32]. Parameters were adjusted in the
630 case of a suboptimal fit compared to the empirical data (pv=60, random_state=1234).
631 The final variograms were used to build and compare null probability for the mean and
632 CoV between BF subregions.

633 To assess the stability of structural and functional connectivity gradients and the
634 gradient of their tethering, we performed split-half and leave-one-out cross-validation
635 analyses across the 173 individuals in the sample (Supplemental Fig. 3). For each split, or
636 subject left out, the model was trained on the remaining individuals, and the predicted
637 gradient was compared to the observed gradient for the left-out individual.

638 Spin tests[37], as implemented in the neuromaps toolbox [44], were used to compare
639 cortical maps based on N=10k permuted maps. All cortical maps were parcellated using
640 the HCP-MMP 1.0 atlas [32] and values were rescaled between 0 and 1 [109]. In addition to
641 the spin tests, a bootstrapping analysis was performed to quantify the difference
642 between structural and functional connectivity and their correlation with [^{18}F]FEOBV
643 PET maps and fiber length. Here, bootstrapping was applied 10k times (by randomly
644 selecting sets of regions during each iteration) to build a null probability of correlation
645 coefficients for statistical inference based on the observed difference between the two
646 modalities.

647 Data and code Availability

648 The Human Connectome (HCP) project dataset is available at
649 http://www.humanconnectomeproject.org/. The workflow for reconstructing structural

connectivity matrix from the HCP data and a subcortical region of interest is available at https://github.com/sudesnac/diffparc-smk [119]; and the functional connectivity workflow at https://github.com/khanlab/subcorticalparc-smk [120]. All other code used to conduct the reported analyses and create the figures are available at https://github.com/sudesnac/HumanBF-Connectivity [121].

Acknowledgments

RH was supported by a BrainsCAN postdoctoral fellowship as well as a Marie Skłodowska-Curie Actions Postdoctoral Fellowship (101061988). This research was enabled in part by the support provided by the Digital Research Alliance (https://alliancecan.ca), and the Natural Sciences and Engineering Research Council (TWS). Data was provided in part by the Human Connectome Project, WU-Minn Consortium (Principal Investigators: David Van Essen and Kamil Ugurbil; 1U54MH091657) funded by the 16 NIH Institutes and Centers that support the NIH Blueprint for Neuroscience Research; and by the McDonnell Center for Systems Neuroscience at Washington University. The PET data used in the analysis was supported by the National Institutes of Health [PO1 NS015655, RO1 NS070856, P50 NS091856, P50 NS123067].

668 **References**

669 1. Mesulam, M. M., Mufson, E. J., Levey, A. I. & Wainer, B. H. Cholinergic innervation
670 of cortex by the basal forebrain: cytochemistry and cortical connections of the
671 septal area, diagonal band nuclei, nucleus basalis (substantia innominata), and
672 hypothalamus in the rhesus monkey. *J. Comp. Neurol.* **214**, 170–197 (1983).
673 2. Li, A. *et al.* Generation of a whole-brain atlas for the cholinergic system and
674 mesoscopic projectome analysis of basal forebrain cholinergic neurons.
675 *Proceedings of the National Academy of Sciences* **115**, 415–420 (2017).
676 3. Do, J. P. *et al.* Cell type-specific long-range connections of basal forebrain circuit.
677 *Elife* **5**, (2016).
678 4. Wu, H., Williams, J. & Nathans, J. Complete morphologies of basal forebrain
679 cholinergic neurons in the mouse. *Elife* **3**, e02444 (2014).
680 5. Muñoz, W. & Rudy, B. Spatiotemporal specificity in cholinergic control of
681 neocortical function. *Curr. Opin. Neurobiol.* **26**, 149–160 (2014).
682 6. Gielow, M. R. & Zaborszky, L. The Input-Output Relationship of the Cholinergic
683 Basal Forebrain. *Cell Rep.* **18**, 1817–1830 (2017).
684 7. Zaborszky, L. *et al.* Neurons in the basal forebrain project to the cortex in a complex
685 topographic organization that reflects corticocortical connectivity patterns: An
686 experimental study based on retrograde tracing and 3D reconstruction. *Cereb.*
687 *Cortex* **25**, 118–137 (2015).
688 8. Yuan, R., Biswal, B. B. & Zaborszky, L. Functional Subdivisions of Magnocellular Cell

689 Groups in Human Basal Forebrain: Test-Retest Resting-State Study at Ultra-high
690 Field, and Meta-analysis. *Cereb. Cortex* **29**, 2844–2858 (2019).
691 9. Markello, R. D., Spreng, R. N., Luh, W. M., Anderson, A. K. & De Rosa, E. Segregation
692 of the human basal forebrain using resting state functional MRI. *Neuroimage* **173**,
693 287–297 (2018).
694 10. Fritz, H. C. J. *et al.* The corticotopic organization of the human basal forebrain as
695 revealed by regionally selective functional connectivity profiles. *Hum. Brain Mapp.*
696 **40**, 868–878 (2019).
697 11. Schmitz, T. W., Mur, M., Aghourian, M., Bedard, M. A. & Spreng, R. N. Longitudinal
698 Alzheimer's Degeneration Reflects the Spatial Topography of Cholinergic Basal
699 Forebrain Projections. *Cell Rep.* **24**, 38–46 (2018).
700 12. Kilimann, I. *et al.* Subregional basal forebrain atrophy in alzheimer's disease: A
701 multicenter study. *J. Alzheimers. Dis.* **40**, 687–700 (2014).
702 13. Scheef, L. *et al.* Subregional volume reduction of the cholinergic forebrain in
703 subjective cognitive decline (SCD). *Neuroimage Clin* **21**, 101612 (2019).
704 14. Nemy, M. *et al.* Cholinergic white matter pathways make a stronger contribution to
705 attention and memory in normal aging than cerebrovascular health and nucleus
706 basalis of Meynert. *Neuroimage* 116607 (2020).
707 15. Teipel, S. J. *et al.* Brain atrophy in primary progressive aphasia involves the
708 cholinergic basal forebrain and Ayala's nucleus. *Psychiatry Res.* **221**, 187–194
709 (2014).

710 16. Fernández-Cabello, S. *et al.* Basal forebrain volume reliably predicts the cortical
711 spread of Alzheimer's degeneration. *Brain* **143**, 993–1009 (2020).
712 17. Van Essen, D. C. *et al.* NeuroImage The WU-Minn Human Connectome Project : An
713 overview. *Neuroimage* **80**, 62–79 (2013).
714 18. Schotten, M. T. de, de Schotten, M. T., Alves, P. N., Corbetta, M. & Forkel, S. The
715 subcortical and neurochemical organization of the ventral and dorsal attention
716 networks. Preprint at https://doi.org/10.21203/rs.3.rs-1804139/v1.
717 19. Corbetta, M., Patel, G. & Shulman, G. L. The reorienting system of the human brain:
718 from environment to theory of mind. *Neuron* **58**, 306–324 (2008).
719 20. Uddin, L. Q. Salience processing and insular cortical function and dysfunction. *Nat.*
720 *Rev. Neurosci.* **16**, 55–61 (2015).
721 21. Uddin, L. Q., Yeo, B. T. T. & Spreng, R. N. Towards a Universal Taxonomy of Macro-
722 scale Functional Human Brain Networks. *Brain Topogr.* **32**, 926–942 (2019).
723 22. Menon, V. & Uddin, L. Q. Saliency, switching, attention and control: a network
724 model of insula function. *Brain Struct. Funct.* **214**, 655–667 (2010).
725 23. Seeley, W. W. *et al.* Dissociable intrinsic connectivity networks for salience
726 processing and executive control. *J. Neurosci.* **27**, 2349–2356 (2007).
727 24. Seeley, W. W. The Salience Network: A Neural System for Perceiving and
728 Responding to Homeostatic Demands. *J. Neurosci.* **39**, 9878–9882 (2019).
729 25. Yeo, B. T. T. *et al.* The organization of the human cerebral cortex estimated by
730 intrinsic functional connectivity. *J. Neurophysiol.* **106**, 1125–1165 (2011).

731 26. Sridharan, D., Levitin, D. J. & Menon, V. A critical role for the right fronto-insular
732 cortex in switching between central-executive and default-mode networks. *Proc.*
733 *Natl. Acad. Sci. U. S. A.* **105**, 12569–12574 (2008).
734 27. Glasser, M. F. *et al.* The minimal preprocessing pipelines for the Human
735 Connectome Project. *Neuroimage* **80**, 105–124 (2013).
736 28. Zaborszky, L. *et al.* Stereotaxic probabilistic maps of the magnocellular cell groups
737 in human basal forebrain. *Neuroimage* **42**, 1127–1141 (2008).
738 29. Glasser, M. F. *et al.* A multi-modal parcellation of human cerebral cortex. *Nature*
739 *Publishing Group* **536**, 171–178 (2016).
740 30. Selden, N. R., Gitelman, D. R. & Mesulam, M.-M. Trajectories Of Corticopetal
741 Cholinergic Pathways Within The Cerebral Hemispheres Of The Human Brain.
742 *Neuroimage* **7**, S26 (1998).
743 31. Nemy, M. *et al.* Cholinergic white matter pathways along the Alzheimer's disease
744 continuum. *Brain* **146**, 2075–2088 (2023).
745 32. Vos de Wael, R. *et al.* BrainSpace: a toolbox for the analysis of macroscale gradients
746 in neuroimaging and connectomics datasets. *Commun Biol* **3**, 103 (2020).
747 33. Katsumi, Y. *et al.* Correspondence of functional connectivity gradients across
748 human isocortex, cerebellum, and hippocampus. *Commun Biol* **6**, 401 (2023).
749 34. Satopaa, V., Albrecht, J., Irwin, D. & Raghavan, B. Finding a 'Kneedle' in a Haystack:
750 Detecting Knee Points in System Behavior. in *2011 31st International Conference on*
751 *Distributed Computing Systems Workshops* 166–171 (IEEE, 2011).

752 35. Prado, V. F., Roy, A., Kolisnyk, B., Gros, R. & Prado, M. A. Regulation of cholinergic
753 activity by the vesicular acetylcholine transporter. *Biochem. J* **450**, 265–274 (2013).
754 36. Kanel, P., van der Zee, S. & Sanchez-Catasus, C. A. Cerebral topography of vesicular
755 cholinergic transporter changes in neurologically intact adults: A [18F] FEOBV PET
756 study. *Aging brain* (2022).
757 37. Alexander-Bloch, A. F. *et al.* On testing for spatial correspondence between maps
758 of human brain structure and function. *Neuroimage* **178**, 540–551 (2018).
759 38. Aghourian, M. *et al.* Quantification of brain cholinergic denervation in Alzheimer's
760 disease using PET imaging with [18F]-FEOBV. *Mol. Psychiatry* **22**, 1531–1538 (2017).
761 39. Bedard, M.-A. *et al.* Brain cholinergic alterations in idiopathic REM sleep behaviour
762 disorder: a PET imaging study with 18F-FEOBV. *Sleep Med.* **58**, 35–41 (2019).
763 40. Markello, R. D. *et al.* neuromaps: structural and functional interpretation of brain
764 maps. *Nat. Methods* (2022) doi:10.1038/s41592-022-01625-w.
765 41. Chklovskii, D. B. & Koulakov, A. A. Maps in the brain: what can we learn from them?
766 *Annu. Rev. Neurosci.* **27**, 369–392 (2004).
767 42. Bassett, D. S. *et al.* Efficient physical embedding of topologically complex
768 information processing networks in brains and computer circuits. *PLoS Comput.*
769 *Biol.* **6**, e1000748 (2010).
770 43. Bullmore, E. & Sporns, O. The economy of brain network organization. *Nat. Rev.*
771 *Neurosci.* **13**, 336–349 (2012).
772 44. Markello, R. D. *et al.* neuromaps: structural and functional interpretation of brain

773 maps. *bioRxiv* 2022.01.06.475081 (2022) doi:10.1101/2022.01.06.475081.

774 45. Gollo, L. L. *et al.* Fragility and volatility of structural hubs in the human

775 connectome. *Nat. Neurosci.* **21**, 1107–1116 (2018).

776 46. Roberts, J. A. *et al.* The contribution of geometry to the human connectome.

777 *Neuroimage* **124**, 379–393 (2016).

778 47. Oh, S. W. *et al.* A mesoscale connectome of the mouse brain. *Nature* **508**, 207–214

779 (2014).

780 48. Sforazzini, F., Schwarz, A. J., Galbusera, A., Bifone, A. & Gozzi, A. Distributed BOLD

781 and CBV-weighted resting-state networks in the mouse brain. *Neuroimage* **87**, 403–

782 415 (2014).

783 49. Mandino, F. *et al.* A triple-network organization for the mouse brain. *Mol.*

784 *Psychiatry* **27**, 865–872 (2022).

785 50. Fox, M. D. *et al.* The human brain is intrinsically organized into dynamic,

786 anticorrelated functional networks. *Proc. Natl. Acad. Sci. U. S. A.* **102**, 9673–9678

787 (2005).

788 51. Fransson, P. Spontaneous low-frequency BOLD signal fluctuations: an fMRI

789 investigation of the resting-state default mode of brain function hypothesis. *Hum.*

790 *Brain Mapp.* **26**, 15–29 (2005).

791 52. Golland, Y., Golland, P., Bentin, S. & Malach, R. Data-driven clustering reveals a

792 fundamental subdivision of the human cortex into two global systems.

793 *Neuropsychologia* **46**, 540–553 (2008).

794 53. Tian, L. *et al.* The relationship within and between the extrinsic and intrinsic
795 systems indicated by resting state correlational patterns of sensory cortices.
796 *Neuroimage* **36**, 684–690 (2007).
797 54. Greicius, M. D. & Menon, V. Default-mode activity during a passive sensory task:
798 uncoupled from deactivation but impacting activation. *J. Cogn. Neurosci.* **16**, 1484–
799 1492 (2004).
800 55. Doucet, G. *et al.* Brain activity at rest: a multiscale hierarchical functional
801 organization. *J. Neurophysiol.* **105**, 2753–2763 (2011).
802 56. Vincent, J. L., Kahn, I., Snyder, A. Z., Raichle, M. E. & Buckner, R. L. Evidence for a
803 frontoparietal control system revealed by intrinsic functional connectivity. *J.*
804 *Neurophysiol.* **100**, 3328–3342 (2008).
805 57. Spreng, R. N., Stevens, W. D., Chamberlain, J. P., Gilmore, A. W. & Schacter, D. L.
806 Default network activity, coupled with the frontoparietal control network, supports
807 goal-directed cognition. *Neuroimage* **53**, 303–317 (2010).
808 58. Chakraborty, S. *et al.* Focal acetylcholinergic modulation of the human midcingulo-
809 insular network during attention: Meta-analytic neuroimaging and behavioral
810 evidence. *J. Neurochem.* (2023) doi:10.1111/jnc.15990.
811 59. Everitt, B. J. & Robbins, T. W. Central cholinergic systems and cognition. *Annu. Rev.*
812 *Psychol.* **48**, 649–684 (1997).
813 60. Sarter, M., Hasselmo, M. E., Bruno, J. P. & Givens, B. Unraveling the attentional
814 functions of cortical cholinergic inputs: interactions between signal-driven and

815 cognitive modulation of signal detection. *Brain Res. Brain Res. Rev.* **48**, 98–111
816 (2005).
817 61. Sarter, M. & Lustig, C. Forebrain Cholinergic Signaling: Wired and Phasic, Not Tonic,
818 and Causing Behavior. *J. Neurosci.* **40**, 712–719 (2020).
819 62. Schmitz, T. W. & Duncan, J. Normalization and the Cholinergic Microcircuit: A
820 Unified Basis for Attention. *Trends Cogn. Sci.* **22**, 422–437 (2018).
821 63. Krabbe, S. *et al.* Adaptive disinhibitory gating by VIP interneurons permits
822 associative learning. *Nat. Neurosci.* **22**, 1834–1843 (2019).
823 64. Kuchibhotla, K. V. *et al.* Parallel processing by cortical inhibition enables context-
824 dependent behavior. *Nat. Neurosci.* **20**, 62–71 (2017).
825 65. Chen, N., Sugihara, H. & Sur, M. An acetylcholine-activated microcircuit drives
826 temporal dynamics of cortical activity. *Nat. Neurosci.* **18**, 892–902 (2015).
827 66. Xue, M., Atallah, B. V. & Scanziani, M. Equalizing excitation–inhibition ratios across
828 visual cortical neurons. *Nature* **511**, 596–600 (2014).
829 67. Fu, Y. *et al.* A cortical circuit for gain control by behavioral state. *Cell* **156**, 1139–
830 1152 (2014).
831 68. Lee, S. H. *et al.* Activation of specific interneurons improves V1 feature selectivity
832 and visual perception. *Nature* **488**, 379–383 (2012).
833 69. Pi, H.-J. *et al.* Cortical interneurons that specialize in disinhibitory control. *Nature*
834 **503**, 521–524 (2013).
835 70. Pfeffer, C. K., Xue, M., He, M., Huang, Z. J. & Scanziani, M. Inhibition of inhibition in

836 visual cortex: the logic of connections between molecularly distinct interneurons.
837 *Nat. Neurosci.* **16**, 1068–1076 (2013).
838 71. Alitto, H. J. & Dan, Y. Cell-type-specific modulation of neocortical activity by basal
839 forebrain input. *Front. Syst. Neurosci.* **6**, 79 (2012).
840 72. Helmstaedter, M., Sakmann, B. & Feldmeyer, D. Neuronal correlates of local,
841 lateral, and translaminar inhibition with reference to cortical columns. *Cereb.*
842 *Cortex* **19**, 926–937 (2009).
843 73. Miller, J.-E. K., Ayzenshtat, I., Carrillo-Reid, L. & Yuste, R. Visual stimuli recruit
844 intrinsically generated cortical ensembles. *Proc. Natl. Acad. Sci. U. S. A.* **111**, E4053–
845 61 (2014).
846 74. Desimone, R. & Duncan, J. Neural mechanisms of selective visual attention. *Annu.*
847 *Rev. Neurosci.* **18**, 193–222 (1995).
848 75. Reynolds, J. H. & Heeger, D. J. The normalization model of attention. *Neuron* **61**,
849 168–185 (2009).
850 76. Carandini, M. & Heeger, D. J. Normalization as a canonical neural computation.
851 *Nat. Rev. Neurosci.* **13**, 51–62 (2011).
852 77. Záborszky, L. *et al.* Specific Basal Forebrain–Cortical Cholinergic Circuits Coordinate
853 Cognitive Operations. *J. Neurosci.* **38**, 9446–9458 (2018).
854 78. Laszlovszky, T. *et al.* Distinct synchronization, cortical coupling and behavioral
855 function of two basal forebrain cholinergic neuron types. *Nat. Neurosci.* **23**, 992–
856 1003 (2020).

857 79. Shine, J. M. Neuromodulatory Influences on Integration and Segregation in the
858 Brain. *Trends Cogn. Sci.* **23**, 572–583 (2019).
859 80. Singer, W. *et al.* Neuronal assemblies: necessity, signature and detectability. *Trends*
860 *Cogn. Sci.* **1**, 252–261 (1997).
861 81. Fries, P. Neuronal gamma-band synchronization as a fundamental process in
862 cortical computation. *Annu. Rev. Neurosci.* **32**, 209–224 (2009).
863 82. Canolty, R. T. *et al.* Oscillatory phase coupling coordinates anatomically dispersed
864 functional cell assemblies. *Proc. Natl. Acad. Sci. U. S. A.* **107**, 17356–17361 (2010).
865 83. Buzsáki, G. Neural syntax: cell assemblies, synapsembles, and readers. *Neuron* **68**,
866 362–385 (2010).
867 84. Duncan, J. The structure of cognition: attentional episodes in mind and brain.
868 *Neuron* **80**, 35–50 (2013).
869 85. Mattson, M. P. & Magnus, T. Ageing and neuronal vulnerability. *Nat. Rev. Neurosci.*
870 **7**, 278–294 (2006).
871 86. Saxena, S. & Caroni, P. Selective neuronal vulnerability in neurodegenerative
872 diseases: from stressor thresholds to degeneration. *Neuron* **71**, 35–48 (2011).
873 87. Roussarie, J.-P. *et al.* Selective Neuronal Vulnerability in Alzheimer's Disease: A
874 Network-Based Analysis. *Neuron* **107**, 821–835.e12 (2020).
875 88. Schmitz, T. W. & Spreng, R. N. Basal forebrain degeneration precedes and predicts
876 the cortical spread of Alzheimer's pathology. *Nat. Commun.* **7**, 13249 (2016).
877 89. Maier-Hein, K. H. *et al.* Author Correction: The challenge of mapping the human

878 connectome based on diffusion tractography. *Nat. Commun.* **10**, 5059 (2019).
879 90. Vu, A. T. *et al.* High resolution whole brain diffusion imaging at 7T for the Human
880 Connectome Project. *Neuroimage* **122**, 318–331 (2015).
881 91. T Vu, A. *et al.* Tradeoffs in pushing the spatial resolution of fMRI for the 7T Human
882 Connectome Project. *Neuroimage* **154**, 23–32 (2017).
883 92. Mölder, F. *et al.* Sustainable data analysis with Snakemake. *F1000Res.* **10**, 33
884 (2021).
885 93. Kluyver, T. *et al.* Jupyter Notebooks – a publishing format for reproducible
886 computational workflows. in *Positioning and Power in Academic Publishing:*
887 *Players, Agents and Agendas* (eds. Loizides, F. & Scmidt, B.) 87–90 (IOS Press,
888 2016).
889 94. Mugler, J. P., 3rd & Brookeman, J. R. Three-dimensional magnetization-prepared
890 rapid gradient-echo imaging (3D MP RAGE). *Magn. Reson. Med.* **15**, 152–157
891 (1990).
892 95. March, 1. WU-Minn HCP 1200 subjects data release reference manual.
893 https://www.humanconnectome.org/storage/app/media/documentation/s1200/H
894 CP_S1200_Release_Reference_Manual.pdf (2018).
895 96. Collins, D. L., Neelin, P., Peters, T. M. & Evans, A. C. Automatic 3D intersubject
896 registration of MR volumetric data in standardized Talairach space. *J. Comput.*
897 *Assist. Tomogr.* **18**, 192–205 (1994).
898 97. Mesulam, M. M., Mufson, E. J., Wainer, B. H. & Levey, A. I. Central cholinergic

899 pathways in the rat: an overview based on an alternative nomenclature (Ch1-Ch6).
900 *Neuroscience* **10**, 1185–1201 (1983b).
901 98. *HCPpipelines: Processing pipelines for the HCP*. (Github).
902 99. Behrens, T. E. J., Berg, H. J., Jbabdi, S., Rushworth, M. F. S. & Woolrich, M. W.
903 Probabilistic diffusion tractography with multiple fibre orientations: What can we
904 gain? *Neuroimage* **34**, 144–155 (2007).
905 100. Grabner, G. *et al.* Symmetric Atlasing and Model Based Segmentation: An
906 Application to the Hippocampus in Older Adults. in *Medical Image Computing and*
907 *Computer-Assisted Intervention – MICCAI 2006* 58–66 (Springer Berlin Heidelberg,
908 2006).
909 101. Griffanti, L. *et al.* ICA-based artefact removal and accelerated fMRI acquisition for
910 improved resting state network imaging. *Neuroimage* **95**, 232–247 (2014).
911 102. Dickie, E. W. *et al.* Ciftify: A framework for surface-based analysis of legacy MR
912 acquisitions. *Neuroimage* **197**, 818–826 (2019).
913 103. Glasser, M. F. *et al.* The Human Connectome Project's neuroimaging approach. *Nat.*
914 *Neurosci.* **19**, 1175–1187 (2016).
915 104. Tian, Y., Margulies, D. S., Breakspear, M. & Zalesky, A. Topographic organization of
916 the human subcortex unveiled with functional connectivity gradients. *Nat.*
917 *Neurosci.* **23**, 1421–1432 (2020).
918 105. Coifman, R. R. *et al.* Geometric diffusions as a tool for harmonic analysis and
919 structure definition of data: diffusion maps. *Proc. Natl. Acad. Sci. U. S. A.* **102**,

920 7426–7431 (2005).

921 106. Katsumi, Y. *et al.* Functional connectivity gradients as a common neural

922 architecture for predictive processing in the human brain. *bioRxiv*

923 2021.09.01.456844 (2021) doi:10.1101/2021.09.01.456844.

924 107. Byrge, L. & Kennedy, D. P. High-accuracy individual identification using a 'thin slice'

925 of the functional connectome. *Netw Neurosci* **3**, 363–383 (2019).

926 108. Kanel, P. *et al.* Cerebral topography of vesicular cholinergic transporter changes in

927 neurologically intact adults: A [18F]FEOBV PET study. *Aging Brain* **2**, 100039 (2022).

928 109. Pedregosa, F. *et al.* Scikit-learn: Machine Learning in Python. *J. Mach. Learn. Res.*

929 **12**, 2825–2830 (2011).

930 110. de Castro, B. M. *et al.* The vesicular acetylcholine transporter is required for

931 neuromuscular development and function. *Mol. Cell. Biol.* **29**, 5238–5250 (2009).

932 111. Logan, J. *et al.* Graphical Analysis of Reversible Radioligand Binding from Time—

933 Activity Measurements Applied to [N-11C-Methyl]-(−)-Cocaine PET Studies in

934 Human Subjects. *J. Cereb. Blood Flow Metab.* **10**, 740–747 (1990).

935 112. Bertoglio, D. *et al.* Validation and noninvasive kinetic modeling of [11C]UCB-J PET

936 imaging in mice. *J. Cereb. Blood Flow Metab.* **40**, 1351–1362 (2020).

937 113. Naumova, A. V., Akulov, A. E., Khodanovich, M. Y. & Yarnykh, V. L. High-resolution

938 three-dimensional macromolecular proton fraction mapping for quantitative

939 neuroanatomical imaging of the rodent brain in ultra-high magnetic fields.

940 *Neuroimage* **147**, 985–993 (2017).

114. Hikishima, K. *et al.* In vivo microscopic voxel-based morphometry with a brain template to characterize strain-specific structures in the mouse brain. *Sci. Rep.* **7**, 85 (2017).

115. Li, C., Gore, J. C. & Davatzikos, C. Multiplicative intrinsic component optimization (MICO) for MRI bias field estimation and tissue segmentation. *Magn. Reson. Imaging* **32**, 913–923 (2014).

116. Ashburner, J. & Friston, K. J. Diffeomorphic registration using geodesic shooting and Gauss–Newton optimisation. *Neuroimage* **55**, 954–967 (2011).

117. Mitchell, J. S. B., Mount, D. M. & Papadimitriou, C. H. The Discrete Geodesic Problem. *SIAM J. Comput.* **16**, 647–668 (1987).

118. Burt, J. B., Helmer, M., Shinn, M., Anticevic, A. & Murray, J. D. Generative modeling of brain maps with spatial autocorrelation. *Neuroimage* **220**, 117038 (2020).

119. Khan, A. & Chakraborty, S. *sudesnac/diffparc-smk: v.0.1.1*. (2023). doi:10.5281/zenodo.7613835.

120. Kai, J., Khan, A. & Chakraborty, S. *subcorticalparc-smk: General-purpose Snakemake workflow for subcortical parcellation with functional and structural connectivity*. (Github). doi:10.5281/zenodo.7622124.

121. Chakraborty, S. *HumanBF-Connectivity*. (Github). doi:https://zenodo.org/badge/latestdoi/599280727.

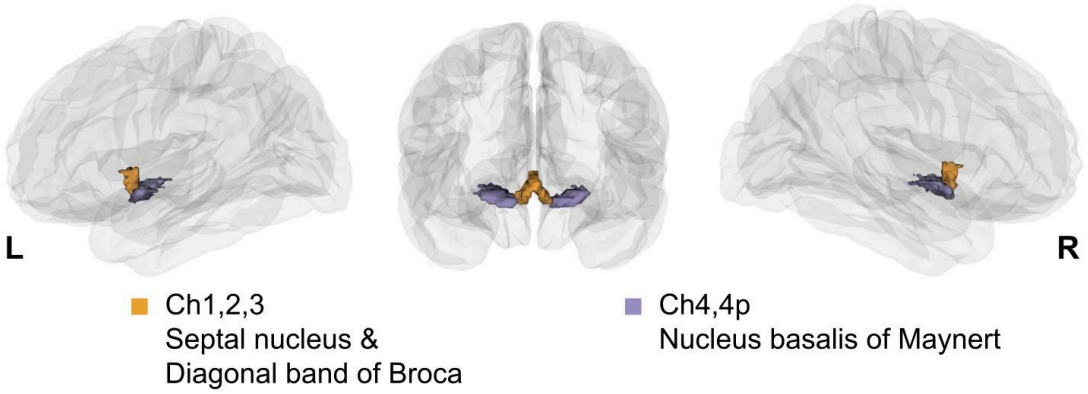

Fig. 1: A 3D view of histologically defined BF subdivisions defined by Zaborsky et al[28] projected on a glass brain. The anteromedial nuclei are displayed in yellow and posterolateral nuclei in purple.

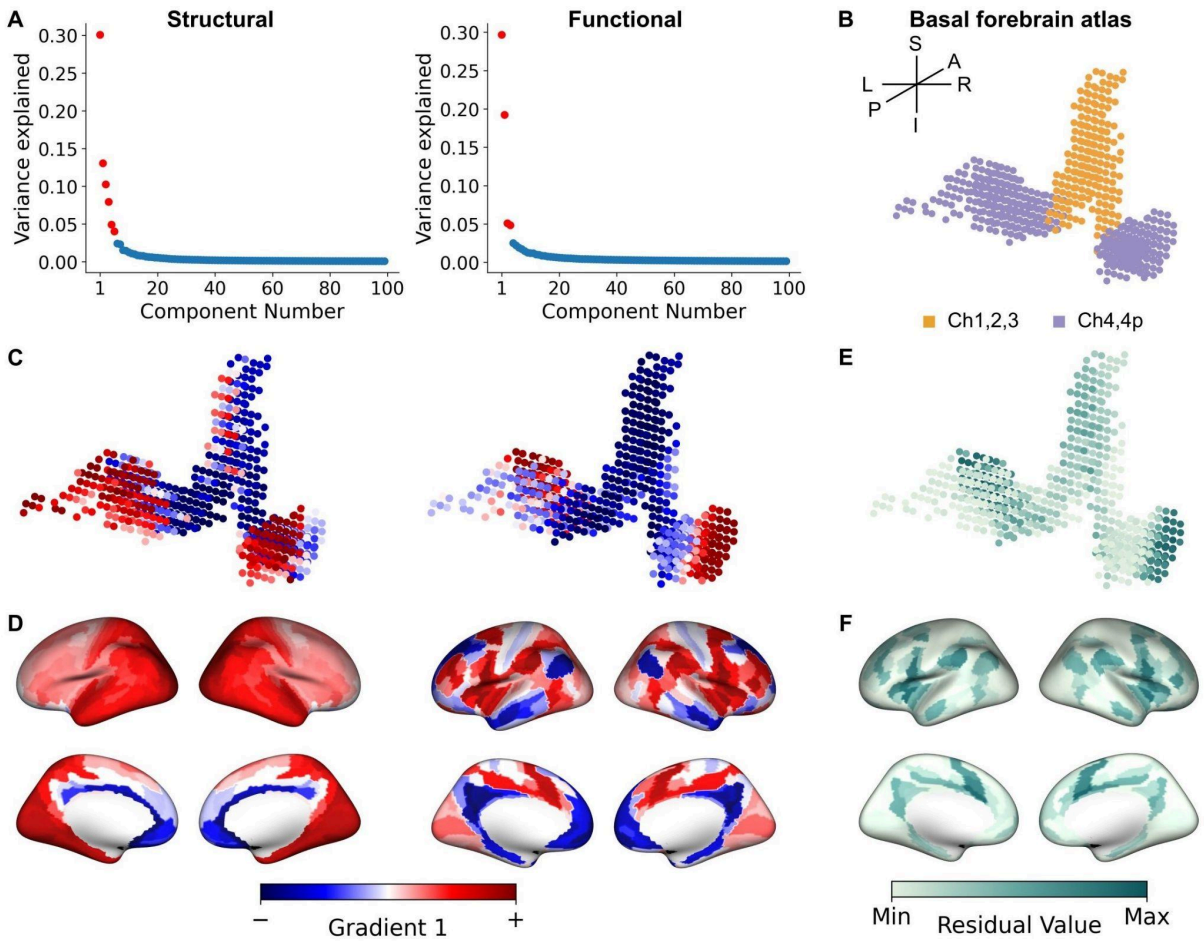

Fig. 2. Basal forebrain (BF) gradients of structural and functional connectivity. (A) Scree plots showing the variance explained by each gradient of structural (left) and functional connectivity (right). Gradients falling above the knee-point[34] are denoted as red. (B) The BF atlas projected into 599 voxels color coded according to a priori histologically defined anteromedial or posterolateral nuclei. (C) The first principal gradient of the BF based on structural (sG1; left) and functional (fG1; right) connectivity both revealed an anteromedial to posterolateral axis. The lower bound of gradient values is represented by blue while the upper bound is represented by red. (D) Gradient-weighted cortical maps corresponding to sG1 (left) and fG1 (right). (E) Residual values encoding tethering between structural and functional connectivity at each BF voxel. Darker green values indicate lower tethering between structural and functional connectivity. (F) Gradient-weighted cortical maps corresponding to structure-function tethering.

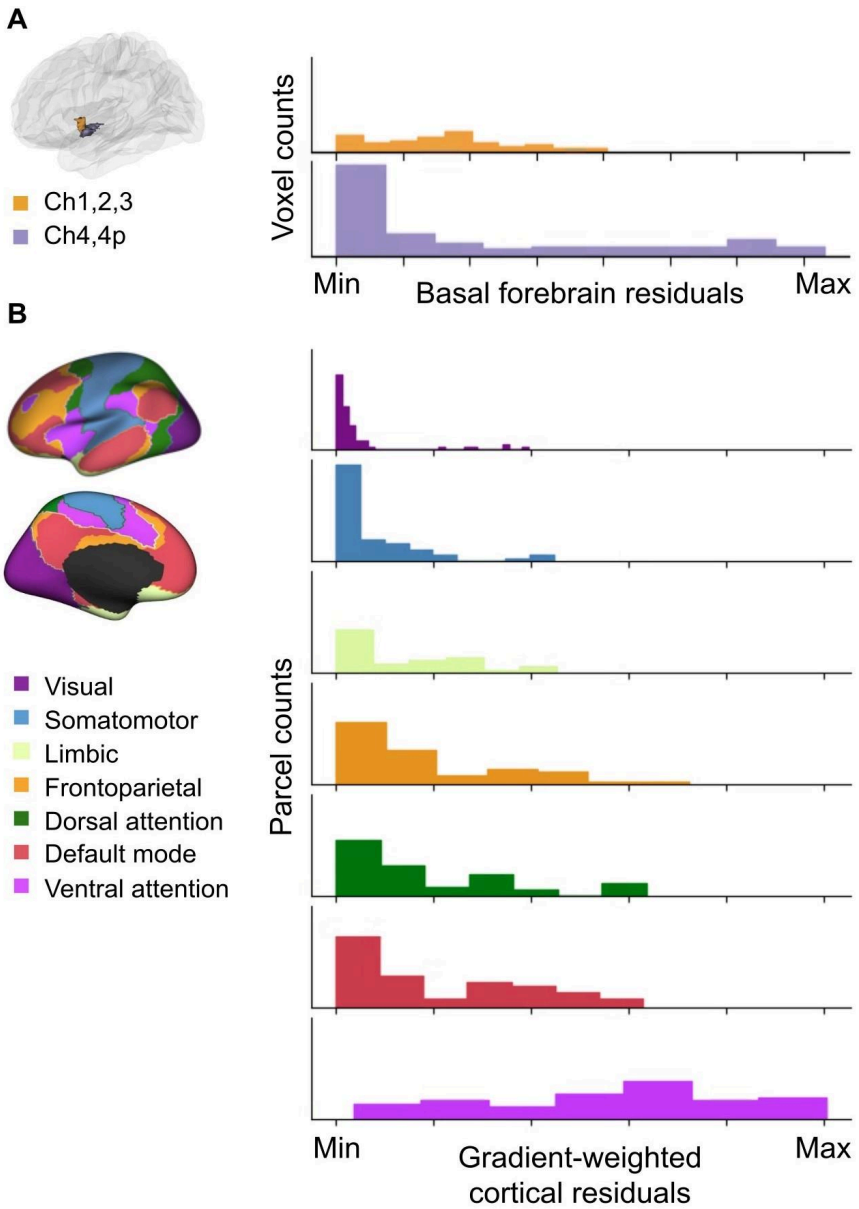

Fig. 3. Distributions of basal forebrain (BF) and cortical residuals. (A) Histogram plot showing the distribution of residuals within the *a priori* histologically defined anteromedial (Ch1,2,3) and posterolateral (Ch4,4p) BF nuclei. The minimum and maximum values correspond to the same scale as in Fig 2E. (B) Histogram plot showing the distribution of residuals within each of the 7 intrinsic resting state networks identified by Yeo et al[25]. The color-coding for different networks is based on the original parcellation. The minimum and maximum values correspond to the same scale as in Fig 2F.

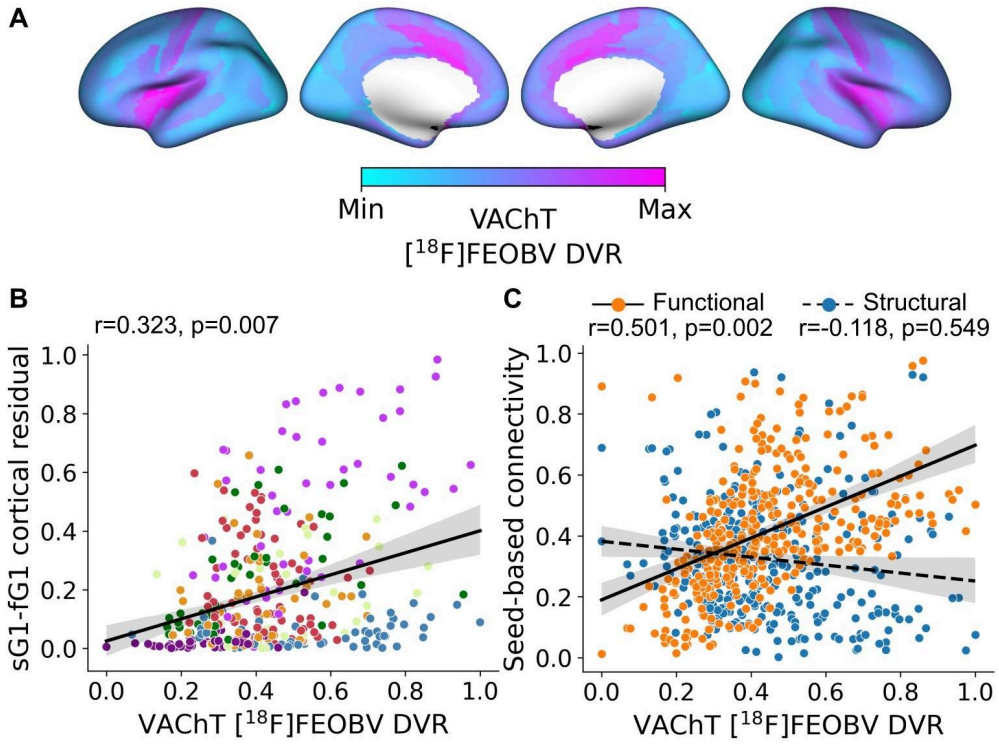

Fig. 4. Multimodal gradients of basal forebrain (BF) connectivity in relation to *in vivo* molecular imaging of VAChT with [^{18}F]FEOBV PET. (A) Average VAChT concentrations for 13 cognitively normal younger adults reveal the density of presynaptic cholinergic terminals across the cortical surface. (B) The spatial relationship of cortical VAChT concentrations (panel A) with the cortical map encoding BF structure-function tethering (Fig 2F). Each point in the scatter plot represents cortical parcels based on HCP-MMP 1.0 parcellation[29] color coded according to the Yeo networks[25] (Fig. 3B). (C) The spatial relationship of cortical VAChT concentrations (panel A) with seed-based connectivity for the BF structural (blue) and functional (orange) datasets.

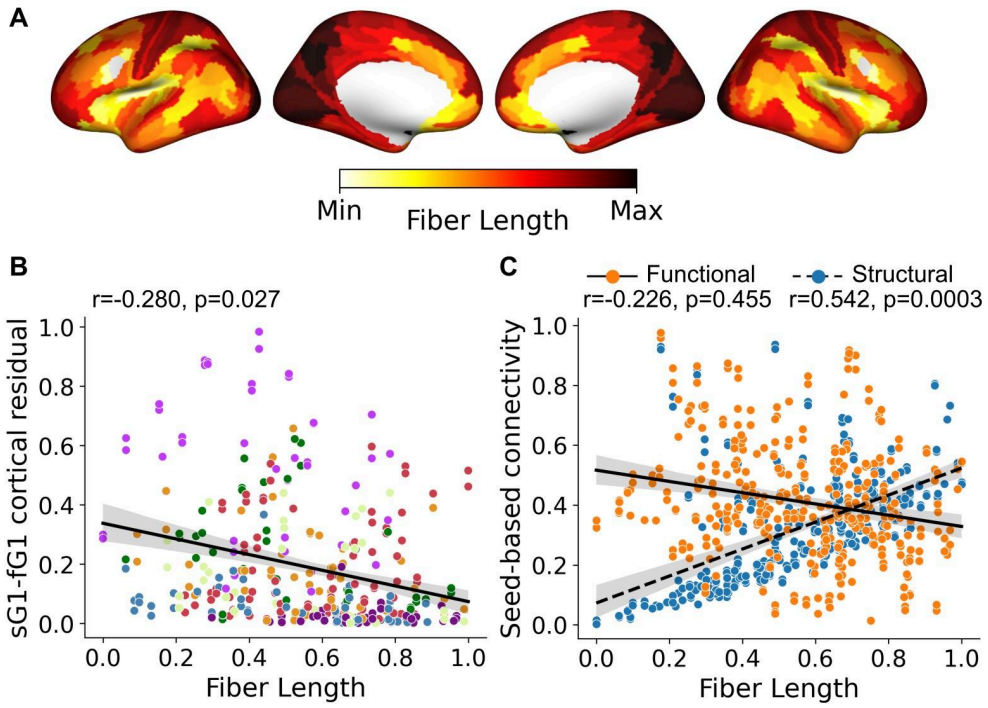

Fig. 5. Multimodal gradients of basal forebrain (BF) connectivity in relation to diffusion tractography estimates of white matter fiber lengths. (A) Average white matter fiber lengths for 173 cognitively normal younger adults reveal cortical areas receiving the longest BF projections located in the primary visual and somatomotor cortices. (B) The spatial relationship of BF white matter fiber lengths (panel A) with the cortical map encoding BF structure-function tethering (Fig 2F). Each point in the scatter plot represents cortical parcels based on HCP-MMP 1.0 parcellation[29] color coded according to the Yeo networks[25] (Fig. 3B). (C) The spatial relationship of BF white matter fiber lengths (panel A) with seed-based connectivity for the BF structural (blue) and functional (orange) datasets.

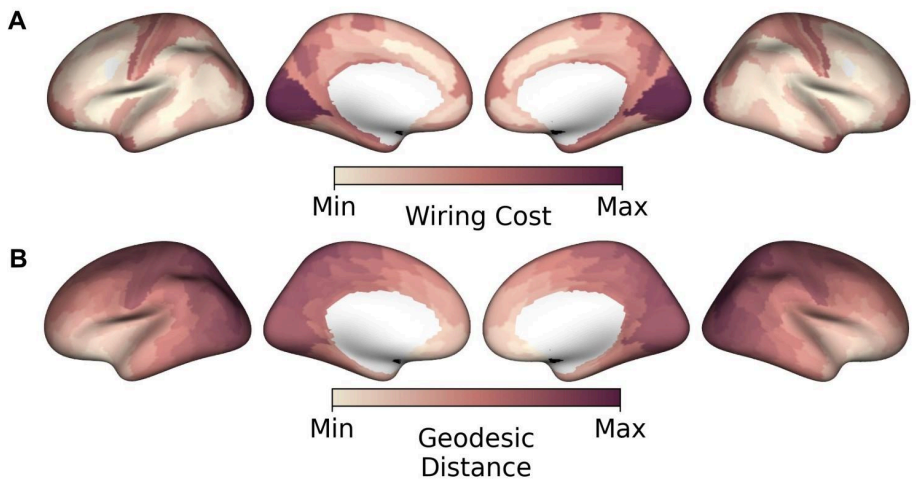

Fig. 6. Cortical wiring costs and geodesic distances for basal forebrain (BF) projections. (A) Wiring costs represent the BF white matter streamline counts for each cortical parcel weighted by their average fiber length[45] (Fig 5A). Wiring costs are highest in primary visual and somatomotor cortices. (B) Geodesic distances from the BF to each parcel on the cortical surface.

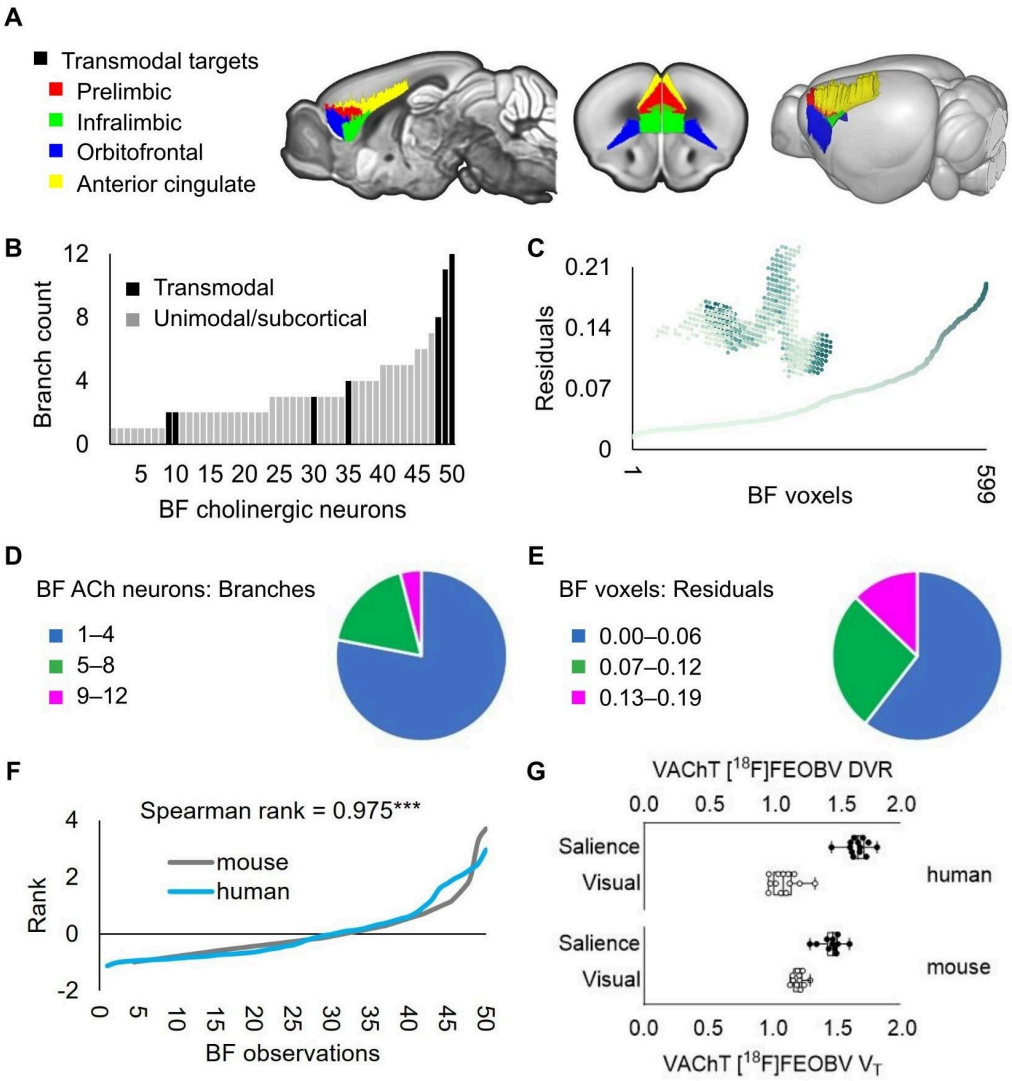

Fig. 7. A cortical gradient of basal forebrain (BF) arborization in mouse and human. (A) In a whole brain atlas of mouse BF cholinergic neurons[2] (n=50) , 7/50 labeled neurons targeted transmodal (iso)cortical areas (color coded on sagittal, coronal and 3D renders of the Allen Mouse Brain Atlas[47] common coordinate framework v3. (B) The number of distinct brain-wide targets for each of the 50 BF cholinergic neurons (branch counts) were ranked low to high (black bars denote neurons targeting transmodal areas, panel A). (C) The residual values encoding BF structure-function tethering in humans across 599 voxels of the BF region-of-interest (inset) were ranked low to high. (D and E) For mouse and human, distributions of neuronal branching and voxel residuals were split into tertiles to examine the concentrations of values (higher versus lower) relative to the total number of observations. (F) The rank ordered residuals across 599 BF voxels (downsampled to 50, blue) are superimposed over the branch counts of 50 mouse neurons (light gray) shown in panel B. (G) Comparisons of *in vivo* [^{18}F]FEOBV PET data between ventral attention and visual networks (human) and between salience network regions (panel A) and a visual cortical control ROI (wild type mice, *n*=11).

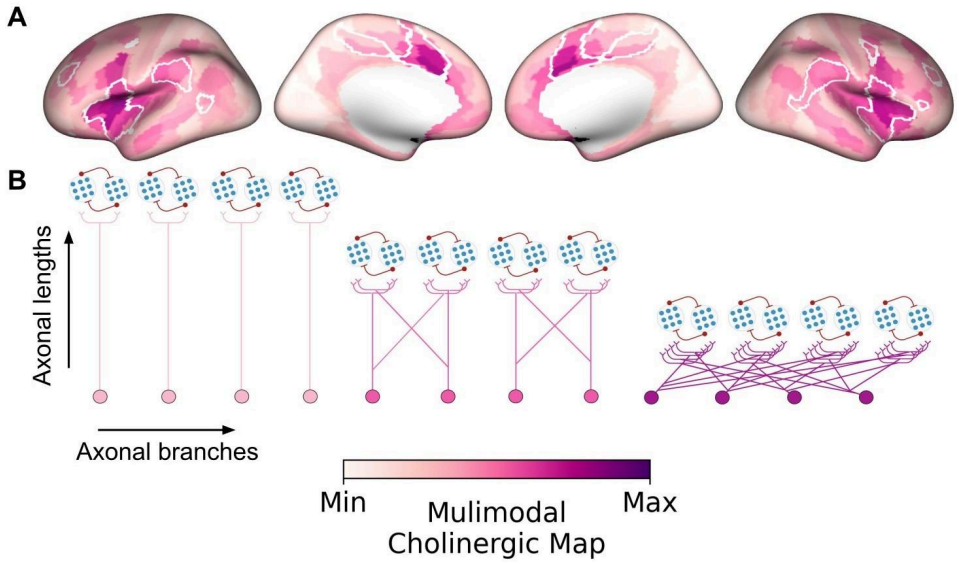

Fig. 8. Multimodal map of the human basal forebrain (BF) cholinergic projectome. (A) A cortical surface emphasizing the arborization gradient of BF cholinergic neurons was constructed by summing the intensity normalized maps encoding (1) BF structure-function tethering (higher values indicate lower tethering), (2) cortical VAChT concentration (higher values indicate higher VAChT), and (3) inverted fiber lengths of BF white matter projections (higher values indicate shorter length). The highest convergence of these three features selectively colocalizes midcingulo-insular hubs of the ventral attention network (white boundaries derived from Yeo et al[25]). (B) Depending on the subregional point of origin within the BF (anteromedial or posterolateral) and cortical target, BF cholinergic neurons may exhibit either a modular (more neurons, fewer branches) or diffuse (fewer neurons, more branches) profile of arborization.